Geophysical Research Letters

Supporting Information for

Airborne Observations Constrain Heterogeneous Nitrogen and Halogen Chemistry on Tropospheric and Stratospheric Biomass Burning Aerosol

Zachary C.J. Decker[1,2,3,a], Gordon A. Novak[1,2], Kenneth Aikin[1,2], Patrick R. Veres[1,b], J. Andrew Neuman[1,2], Ilann Bourgeois[1,2,c], T. Paul Bui[4], Pedro Campuzano-Jost[2,3], Matthew M. Coggon[1,2], Douglas A. Day[2,3], Joshua P. DiGangi[5], Glenn S. Diskin[5], Maximilian Dollner[6], Alessandro Franchin[1,2,7], Carley D. Fredrickson[8], Karl D. Froyd[1,2], Georgios I. Gkatzelis[1,2,d], Hongyu Guo[2,3], Samuel R. Hall[7], Hannah Halliday[5], Katherine Hayden[9], Christopher D. Holmes[9], Jose L. Jimenez[2,3], Agnieszka Kupc[1,2,6], Jakob Lindaas[11], Ann M. Middlebrook[1], Richard H. Moore[5], Benjamin A. Nault[12], John B. Nowak[5], Demetrios Pagonis[2,3,e], Brett B. Palm[8,b], Jeff Peischl[1,2], Felix M. Piel[13,14], Pamela S. Rickly[1,2,f], Michael A. Robinson[1,2,3], Andrew W. Rollins[1], Thomas B. Ryerson[1], Gregory P. Schill[1], Kanako Sekimoto[15], Chelsea R. Thompson[1], Kenneth L. Thornhill[5,16], Joel A. Thornton[8], Kirk Ullmann[7], Carsten Warneke[1], Rebecca A. Washenfelder[1,g], Bernadett Weinzierl[6], Elizabeth B. Wiggins[5], Christina J. Williamson[1,2,h,i], Edward L. Winstead[5,16], Armin Wisthaler[13,14], Caroline C. Womack[1,2], Steven S. Brown[1,3]

[1]NOAA Chemical Sciences Laboratory (CSL), Boulder, Colorado 80305, USA

[2]Cooperative Institute for Research in Environmental Sciences, University of Colorado Boulder, Boulder, Colorado 80309, USA

[3]Department of Chemistry, University of Colorado Boulder, Boulder, Colorado 80309-0215, USA

[4]NASA Ames Research Center, Moffett Field, CA, USA

[5]NASA Langley Research Center, MS 483, Hampton, VA 23681, USA

[6]Faculty of Physics, Aerosol Physics and Environmental Physics, University of Vienna, Vienna, Austria

[7]Atmospheric Chemistry Observations and Modeling Laboratory, National Center for Atmospheric Research, Boulder, CO 80301, USA

[8]Department of Atmospheric Sciences, University of Washington, Seattle, Washington 98195, United States

[9]Air Quality Research Division (AQRD), Environment and Climate Change Canada, Toronto M3H 5T4, Ontario, Canada

[10]Department of Earth, Ocean, and Atmospheric Science, Florida State University, Tallahassee, FL 32306, USA

[11]Department of Atmospheric Science, Colorado State University, Fort Collins, CO 80523, USA

[12]Center for Aerosol and Cloud Chemistry, Aerodyne Research, Inc., Billerica, MA, USA

[13]Institute for Ion Physics and Applied Physics, University of Innsbruck, 6020 Innsbruck, Austria

[14]Department of Chemistry, University of Oslo, 0315 Oslo, Norway

[15]Graduate School of Nanobioscience, Yokohama City University, Yokohama, Kanagawa, 236-0027, Japan

[16]Science Systems and Applications, Inc. (SSAI), Hampton, VA 23666, USA

[a]Now at Laboratory of Atmospheric Chemistry, Paul Scherrer Institute (PSI), 5232 Villigen, Switzerland

[b]now at National Center for Atmospheric Research, Boulder, CO 80301, USA

[c]now at Université Savoie Mont Blanc, INRAE, CARRTEL, 74200 Thonon-les-Bains, France

[d]Now at Institute of Energy and Climate Research, IEK-8: Troposphere, Forschungszentrum Jülich GmbH, Jülich, Germany

[e]now at Department of Chemistry and Biochemistry, Weber State University, Ogden, UT 84408

[f]now at Colorado Department of Public Health and Environment, 4300 Cherry Creek S Dr, Denver, CO 80246

[g]now at Cooperative Institute for Research in Environmental Sciences, University of Colorado Boulder, Boulder, Co 80309, USA

[h]now at Finnish Meteorological Institute, Erik Palmenin Aukio 1, 00560 Helsinki, Finland

[i]now at Institute for Atmospheric and Earth System Research/Physics, Faculty of Science, University of Helsinki, P.O. Box 64, 00014 Helsinki, Finland

Contents of this file

Introduction

The supporting information includes text describing the FIREX-AQ and ATom observations as well as additional details about analysis methods such as box models and parameterizations. It further includes a series of supporting figures and captions

S1 Observations and Models

FIREX-AQ was a large-scale field research campaign focusing on wildfire smoke plumes in the western U.S. and prescribed agricultural burning smoke plumes in the southeastern U.S. during the summer of 2019. We use observations from the NOAA Chemistry Twin Otter and NASA DC-8 aircraft. The NASA Atmospheric Tomography (ATom) mission was a large-scale research campaign focusing on remote tropospheric, UTLS, and stratospheric air [*Thompson et al.*, 2022]. Data here are from September–October 2017 (ATom-3) and April–May 2018 (ATom-4). Table S1 lists instrumentation used in this analysis. In-situ observations from ATom and FIREX-AQ are available as a merged dataset and found in [*Wofsy et al.*, 2018] and [*Warneke et al.*, 2023], respectively. See further details in the SI.

Two models are used: an iterative 0-D box model constrained to crosswind transects of wildfire plumes sampled during FIREX-AQ and an iterative diel model constrained to observations for each parcel of sampled air above an arbitrary elevation cutoff of 6 km during ATom-3 and ATom-4. Calculated $\varphi(ClNO_2)$ uses a parameterization determined from laboratory experiments [*Bertram et al.*, 2009; *Roberts et al.*, 2009]. See further details below.

S1.1 FIREX-AQ Observations

From the Twin Otter, we use a commercial cavity ringdown spectrometer (Picarro) for measurements of CO. We also use measurements of non-refractory PM_1 chemical composition from an Aerosol Mass Spectrometer (AMS) [*Liggio et al.*, 2016].

From the DC-8, we use measurements of CO from a tunable diode laser spectrometer when available and from an integrated cavity output spectrometer when unavailable. Measurement of NO is by laser-induced fluorescence (LIF). Measurements of NO_y and O_3 are provided by a NOAA chemiluminescence (CL) instrument. We use an average measurement of NO_2 from both the NOAA CL instrument and a NOAA cavity-enhanced spectrometer. Measurements of HONO are taken from the NOAA I^- ToF CIMS. Measurements of VOCs are taken from the NOAA I^- ToF CIMS [*Neuman et al.*, 2016; *Veres et al.*, 2020], NOAA Proton Transfer Reaction (PTR) MS [*Koss et al.*, 2018], and the University of Innsbruck PTR-MS [*Müller et al.*, 2014]. Aerosol surface area measurements are taken from a laser aerosol spectrometer (LAS, 1 Hz) for aerosol sizes between 0.1 μm and 5 μm. Measurements of non-refractory PM_1 are from the CU HR-AMS, 1-5 Hz [*Guo et al.*, 2021]. Spectrally resolved actinic flux was measured with separate upward and downward-facing actinic flux optics.

The sensitivity of the iodide CIMS to $ClNO_2$ was determined using methods similar to those described in [*Lao et al.*, 2020]. A Cl_2 mixture (4.167 ppm Cl_2 in 50% RH zero air) was passed through a $NaNO_2$-coated PFA tube to dynamically produce $ClNO_2$:

$$Cl_2\,(g) + NO_2\,(aq)^- \rightarrow ClNO_2\,(aq) + Cl\,(aq)^- \qquad \text{(RS1)}$$

$ClNO_2$ (aq) $\rightarrow$ $ClNO_2$ (g) (RS2)

The source output was calibrated by a chemiluminescence NO_y instrument that measures NO, NO_2 and $ClNO_2$ as NO_y [*Thaler et al.*, 2011]. The calibrated $ClNO_2$ source was then used for calibration of the iodide CIMS.

An N_2O_5 calibration source was produced online via the reaction of O_3 with NO_2 to form N_2O_5 [*Lee et al.*, 2018]. The output of the calibration source was measured using a cavity ring down instrument for direct detection of N_2O_5 [*Wagner et al.*, 2011]. The iodide CIMS was calibrated by comparing the observed signal at $I{\bullet}N_2O_5^-$ to the CRDS determined N_2O_5 concentration.

$ClNO_2$ is reported with a precision of 0.1 ppt for 1s data and accuracy of 15% + 0.05 ppt and N_2O_5 is reported with a precision of 0.1 ppt for 1s data and accuracy of 15% + 2 ppt. We report the precision as the 1 sigma limit of detection based on signal variability during instrument zeroing in flight. The accuracy of these measurements is quantified as a % based on calibration errors in addition to the error associated with variability instrument background determinations. The latter part of this quantity, 0.05 ppt for $ClNO_2$ and 2 ppt for N_2O_5, is defined as the RMS of consecutive background determinations to quantify the error due to linear interpolation between background points. Instrument backgrounds were performed by overflowing the inlet with humidified nitrogen (N_2) for a period of at least 30 seconds every 10 minutes.

S1.2 ATom Observations

Aerosol sizing and composition data incorporate measurements from the CU HR-AMS [*Guo et al.*, 2021] and bulk aerosol size distributions [*Brock et al.*, 2019]. A Cloud, Aerosol, and Precipitation Spectrometer was used to reject periods of sampling within clouds. Measurements of single particle composition and particle mixing states are from a single-particle laser ionization mass spectrometer (PALMS). The amount of pyrogenic influence is a semi-empirical classification based on the relative peak areas of carbon ($^{12}C^+$) and potassium ($^{39}K^+$) [*Schill et al.*, 2020]. Mixing ratios of NO, NO_2, and O_3 were measured with the NOAA CL and measurements of OH and HO_2 were by LIF. Mixing ratio of N_2O_5 was measured by the NOAA I^- ToF CIMS (LoD = 0.1 pptv, 1-σ, 1Hz, Figure S19) [*Veres et al.*, 2020].

S1.3 Box Models

The iterative 0-D box model of wildfire plumes is described in detail by Decker et al. [*Decker et al.*, 2021] and discussed briefly here. We model six smoke plumes from three fires sampled on six separate days (Williams Flats, North Hills, and Shady – see Table S3). Box modeling was performed using the Framework for 0-D Atmospheric Modeling (F0AM) [*Wolfe et al.*, 2016] and includes chemistry from the Master Chemical Mechanism (MCM, v3.3.1 via http://mcm.york.ac.uk, last access: 23 September 2021) [*Bloss et al.*, 2005], with additional BB mechanisms [*Decker et al.*, 2021]. The model considers only transect-center observations defined as the observations which correspond to the greatest 5% of CO enhancements.

The ATom model builds on the framework of previous model determinations of $\gamma(N_2O_5)$ in the lower troposphere constrained by aircraft measurements [*McDuffie et al.*, 2018a], with changes for the ATom flight scheme and distinct conditions of the UTLS

described here. A run is initiated at the time of local sunset prior to the observation for each 10 s data average and run for a 24-hour diel cycle through to the local sunset after the time of each observation, with diel profiles of photolysis rates and OH concentrations constrained to observations. Mixing ratios of long-lived species, such as H_2O and aerosol surface area, are held constant over the 24 h period. The model iterates the initial NO_x until NO is within 20% of observations while NO_2 remains unconstrained. Next, $k_{N_2O_5}$ is iterated until N_2O_5 is within 20% of observations and $\gamma(N_2O_5)$ is calculated from observed temperature and aerosol surface area. We select only data > 6 km that include the required observations for the model above the instrument LoD (77% of data). Of the points modeled, 48% (17,455 determinations) converge on a $k_{N_2O_5}$ between 1×10^{-8} and 1.

S1.4 Parameterization of $\varphi(ClNO_2)$

Production of $ClNO_2$ is considered to proceed by ionization of N_2O_5 to form $NO_2^+ + NO_3^-$. The formation of either HNO_3 or $ClNO_2$ is based on kinetic competition for the reaction of NO_2^+ with H_2O or Cl^-, respectively [*Bertram et al.*, 2009]. Re-formation of N_2O_5 may also be competitive due to significant concentrations of NO_3^- relative to Cl^- (Figure S20). Therefore, this competitive reaction, derived by [*McDuffie et al.*, 2018b] is also included.

$$\Phi(\mathrm{ClNO2}) = \left(k_a \frac{[H_2O]}{[Cl^-]} + k_b \frac{[NO_3^-]}{[Cl^-]} + 1\right)^{-1} \quad \text{(S1)}$$

Here k_a is taken as 2.1×10^{-3} and k_b as 3.4×10^{-2} from the work of Bertram, 2009 #31}. Both k_a and k_b are ratios of solution phase rate constants and therefore unitless.

We use observations of pCl^-, particulate NO_3^- and calculated LWC to calculate $\varphi(ClNO_2)$. The LWC is estimated as the sum of water associated with individual aerosol species [*Guo et al.*, 2015]. The inorganic part is calculated with ISORROPIA-II thermodynamic model [*Fountoukis and Nenes*, 2007] in the forward mode. The inorganic aerosol composition is measured by an AMS, HNO_3 (from CIMS), NH_3 from PTR-MS, RH, and temperature. The organic part is estimated based on the organic aerosol mass concentration, density, and hygroscopicity (κOA) from AMS, in which the κOA is predicted via the organic aerosol oxygen-to-carbon (O/C) ratio [*Rickards et al.*, 2013].

S1.5 Calculation of NEMRs

The NEMRs are calculated by three different methods depending on the observation. NEMRs of pCl^- are calculated by the linear fit of pCl^- vs. CO while results with an $R^2 <$ 0.3 are rejected (11% rejected). NEMRs of N_2O_5 and $ClNO_2$ in Figure 2 are calculated by integrating the analyte and CO for observations > 3-4× the LoD of the analyte based on a transect-by-transect review. Transects with N_2O_5 and $ClNO_2$ below this threshold were rejected (33%). Transect center NEMRs in Figures 3-4 are calculated using transect center observations. The transect center CO value is the average of the top 5 % of CO observations while the transect center analyte value is the analyte observations which align with the top 5 % of CO observations. NEMRs are intended as a metric for the amount of analyte observed relative to the plume size. NEMRs are not equivalent to

emission ratios and are biased by several variables such as plume age, other plume emissions, and fuel type.

Calculation of NEMR values for pCl^-

NEMR values of pCl^- were calculated by linear correlation with CO. All transects for one fire plume were used in the determination of a single NEMR. We use all transects in one determination because we assume pCl^- is an emission with dilution as the main loss process in the young plumes we consider. The slope of the linear fit is taken to be the NEMR. We only consider plumes whose correlation results in an $R^2 > 0.3$. For montane fueled plumes this is 14 out of 16 plumes. For grass fueled plumes this is 83 out of 93.

NEMR values of N_2O_5 and $ClNO_2$ used in Figure 2

NEMR values of N_2O_5 and $ClNO_2$ used for histograms are calculated by integration of individual plume transects as shown by Equation S2.

$$\frac{\int x\,dt - \bar{x} \times \Delta t}{\int CO\,dt - \overline{CO} \times \Delta t} \quad \text{(S2)}$$

Here x is the analyte within the plume, x_{bg} is the average analyte mixing ratio outside of a plume and Δt is the elapsed time over which the analyte and CO were integrated. The region selection criteria is described further below. The integration method is used, as opposed to a correlation method, because $ClNO_2$ and N_2O_5 are not directly emitted. Chemical production of $ClNO_2$ and N_2O_5 from precursors other than CO do not necessarily result in a linear correlation.

Note that NEMRs are only calculated for plume transects when measurements of the analyte and CO are present throughout the entirety of the transect and the analyte is roughly 3-4× greater than the LoD. As we demonstrate below, observations rejected for the NEMR calculation are associated with the smallest plumes sampled during FIREX-AQ and therefore the CO is near background and analyte near or at the LoD. Calculating an NEMR for measurements near or below the LoD is uninformative due to the division of small numbers which inflates or gives nonsensical NEMR values.

As shown in Table S2, roughly 39 % and 56 % of all N_2O_5 and $ClNO_2$ transects (montane plus agricultural) were used for the NEMR calculation.

NEMRs in montane- and agricultural-fueled fires from FIREX-AQ

In a case study of N_2O_5 NEMRs calculated for agricultural fueled-plumes, which had the greatest number of rejected transects due to near or below LoD observations, we show that the calculated median NEMR is consistent with N_2O_5 observations in all agricultural plumes.

The limited number of available N_2O_5 NEMR calculations for agricultural plumes is due to the smaller plume size, relative to montane smoke plumes, and larger LoD, relative to $ClNO_2$. As shown in Figure S2 below, most of the near or at LoD observations have transect center CO mixing ratios (average of the top 5% of CO within a plume) much less than transects with detectable N_2O_5.

Calculation of NEMR values for transect center observations:

Transect center NEMRs are calculated according to Equation S3 below.

$$\frac{\Delta x}{\Delta CO} \quad \text{(S3)}$$

Here, Δ refers to the difference of transect and background observations. Transect center observations are taken to be an average of values corresponding to the top 5% of CO values within a transect: see [*Decker et al.*, 2021]. The 1-σ uncertainty of the average is added to measurement uncertainties in quadrature (the square root of the sum of squares) to produce the error bars presented throughout the manuscript. Data below the LoD (including negative values) are included in these calculations without modification.

Plume transect boundary determination:

- Smoke region:
- The smoke tracer CO is enhanced above the background (> 2-σ).
- The smoke is defined (had a clear departure from and return to background levels of CO).
- The transect sampled smoke for more than five continuous seconds (five data points) which corresponds to a plume width of roughly 650 m based on average aircraft speed for the NASA DC-8.
- Background region
- A 15 second period beginning roughly 30 seconds before the transect region (or less if there is less than 30 seconds between transect samples.
- Does not overlap with a smoke region.

S2 Chloride emissions from montane and agricultural fires

The formation of $ClNO_2$ requires particulate chloride (pCl^-). It is known from field and laboratory measurements that agricultural and grass burning emits more Cl^- per kg of fuel burned (emission factor) when compared to temperate and boreal forest burning [*Ahern et al.*, 2018; *Liu et al.*, 2016; *May et al.*, 2014]. As we show below, observations from the NASA DC-8 and NOAA Twin Otter aircraft (hereafter DC-8 and Twin Otter) during FIREX-AQ are consistent with these results.

Figure S5A shows a flight track of the DC-8 on 24 July when two fires were sampled in contrasting environments, which offers a case study of contrasting fuels. The Shady fire burned in a mountainous region with timber, tall grass, and logging debris fuels, while the Sheep fire burned sage grass, juniper, and sagebrush in a grassland region (Table S3). As shown in Figure S5B, the Shady and Sheep Fire plumes differ in pCl^- by roughly a factor of 10. A linear fit of pCl^- vs. CO indicates the above background enhancement of pCl^- relative to the smoke tracer CO, also called the normalized excess mixing ratio (NEMR). Observations of pCl^- were frequently linearly correlated with CO (89% of plumes had an $R^2 > 0.3$) and above the reported LoD from the Aerosol Mass Spectrometer (AMS) aboard the Twin otter (0.09 μg sm^{-3}) and the AMS aboard the DC-8 (median/average ± σ LoD of 0.09 / 0.13 ± 0.09 for montane-fueled smoke and 0.19 / 0.19 ± 0.08 for agricultural fueled-smoke). Specifically, we observed 0.6 μg sm^{-3} $ppmv^{-1}$ CO for the montane fire and 6.1 μg sm^{-3} $ppmv^{-1}$ CO for the grass fire. The results from the July 24 case study shown here are consistent with all smoke observations from both the Twin Otter and DC-8 during FIREX-AQ. Median pCl^- NEMR for grass and agricultural

fueled smoke was 9.9 μg sm^{-3} $ppmv^{-1}$ (or 8.0 mg g^{-1}), which is within a factor of two of aircraft-derived NEMR from May et al.'s analysis (5.4 mg g^{-1} for an east coast U.S. grass fire) [*May et al.*, 2014] and within the reported variability of aircraft results by [*Liu et al.*, 2016], but less than the range of laboratory grass burns (11.1 – 25.3 mg g^{-1}). These results show that agricultural and grass fuels have greater potential for $ClNO_2$ formation and activation.

Biomass burning chloride emissions likely occur in the form of HCl in the gas phase or as potassium or other salts [*May et al.*, 2014]. We have not carried out thermodynamic modeling of the subsequent chloride partitioning between the gas and aerosol phases. Measurement of gas phase HCl was unavailable from the aircraft during FIREX-AQ. Emission factors and NEMRs derived in this work are therefore lower limits. We note, however, that the NEMR for reduced nitrogen (NH_3) greatly exceeds that of chloride [*Akagi et al.*, 2011] and that chloride is soluble in organic aerosol [*Solomon et al.*, 2023]. Therefore, we expect a large fraction of the available chloride to be present as pCl^-.

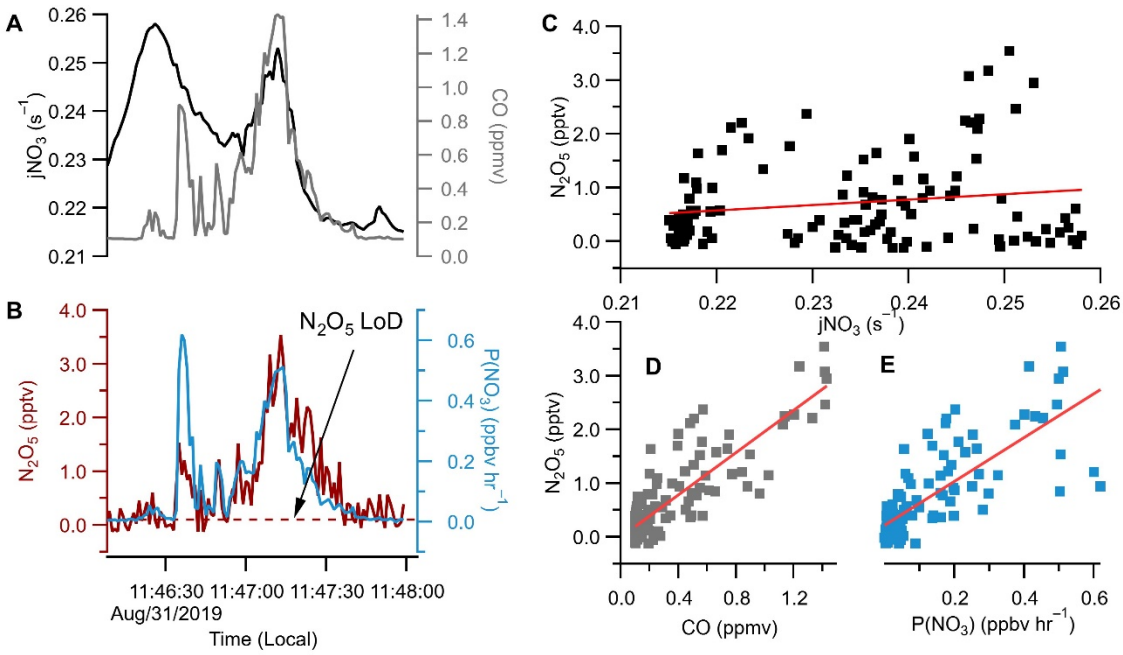

Figure S1. observations taken from a crosswind transect of a small agricultural fire plume at mid-day. (**A**): observations of jNO_3 (left, black) and CO (right, grey). (**B**): observations of N_2O_5 (left, red) and P(NO3) (right, blue). (**C**): correlation plot of N_2O_5 vs. jNO_3 with an $R^2 = 0.03$. (**D**): correlation plot of N_2O_5 vs. CO with an $R^2 = 0.73$. (**E**): correlation plot of N_2O_5 vs. $P(NO_3)$ with an $R^2 = 0.60$.

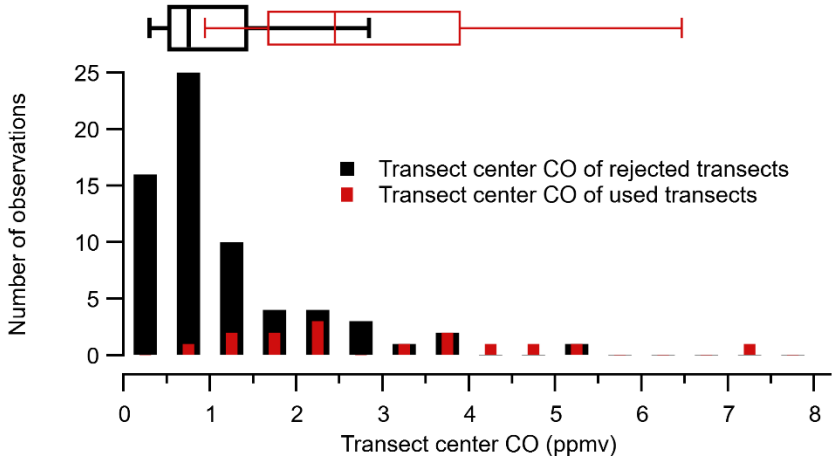

Figure S2. Histogram of transect center CO for transects rejected (black) or used (red) (see Table S2) for NEMR calculations. Box plots show 10th, 25th, 50th, 75th, and 90th percentiles. The median/average ± σ of observations above the LoD is 2.4 / 3.0 ±1.8 and for observations below the LoD it is 0.75 / 1.2 ±1.3. Assuming an NEMR of 1.0 pptv $ppmv^{-1}$ CO (the median result determined in the main text) the expected N_2O_5 mixing ratio shows that the majority of N_2O_5 is expected to be at or below the LoD (Figure S3) and would be rejected by a 3-4× LoD threshold.

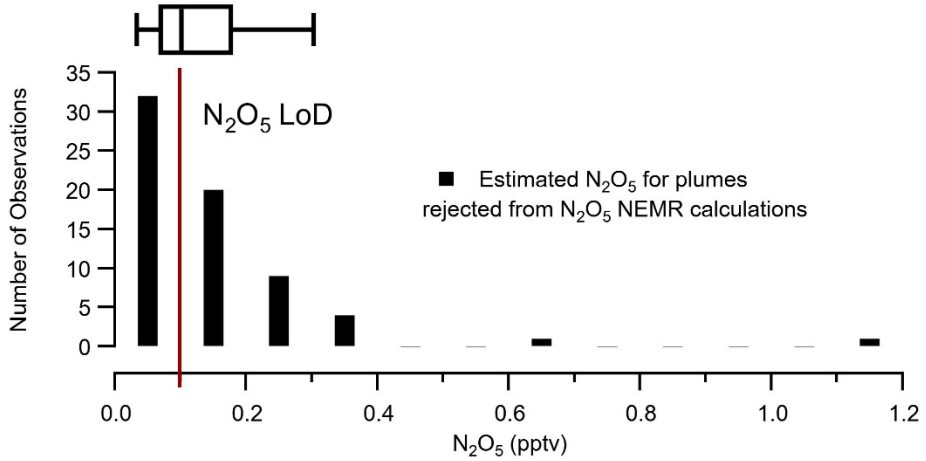

Figure S3. Histogram of estimated N_2O_5 mixing ratio for transects rejected for NEMR calculations. The estimation is based on the observed CO and an NEMR of 1.0 pptv $ppmv^{-1}$ CO as determined in the main text. Box plots show 10^{th}, 25^{th}, 50^{th}, 75^{th}, and 90^{th} percentiles. The median/average ± σ of estimated N_2O_5 mixing ratio is 0.1 / 0.2 ± 0.2

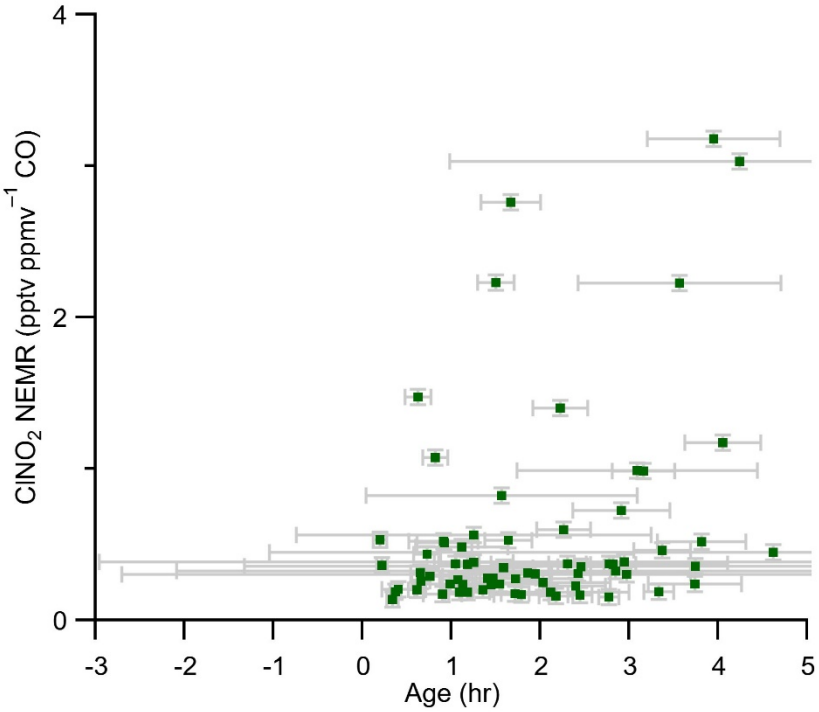

Figure S4. Calculated $ClNO_2$ NEMRs from montane-fueled fires as a function of average plume age.

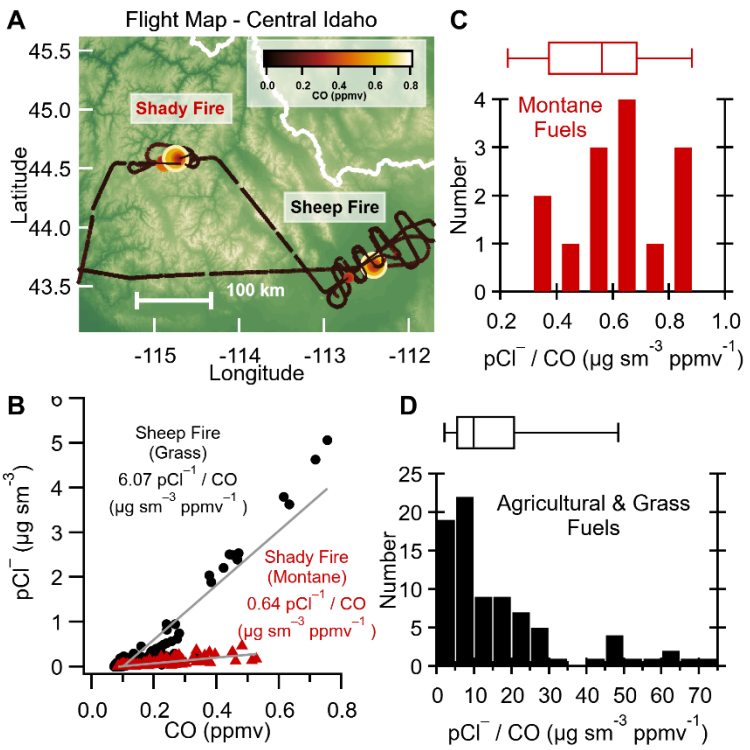

Figure S5. (**A**): flight map (terrain colored by elevation) with the flight path (colored and sized by CO mixing ratio) of the DC-8 sampling the Shady fire plume (red, 17:45–18:15 MDT, including timber, tall grass, and logging debris fuels) and the Sheep fire plume (black, 16:15–16:30 MDT, including sage-grass, juniper, and sagebrush fuels). (**B**) aircraft observations of pCl^- correlated with the CO mixing ratio of the Shady (red, R^2 = 0.62) and Sheep (black, R^2 = 0.87) fire plumes. (**C**) histogram with box and whisker plot of normalized excess mixing ratios of pCl^- for montane fueled smoke observations taken by the DC-8 and the Twin Otter aircraft in FIREX-AQ. (**D**) Similar to panel C but for grass and agricultural fuels. Box plots show 10th, 25th, 50th, 75th, and 90th percentiles. The median NEMR for wildland fuels is 0.6 µg sm^{-3} ppmv^{-1} and the average ± 1-σ is 0.6 ± 0.3 µg sm^{-3} ppmv^{-1}. The median for agricultural fuels is 9.9 µg sm^{-3} ppmv^{-1} and the average ± 1-σ is 16.6 ± 17.1 µg sm^{-3} ppmv^{-1}.

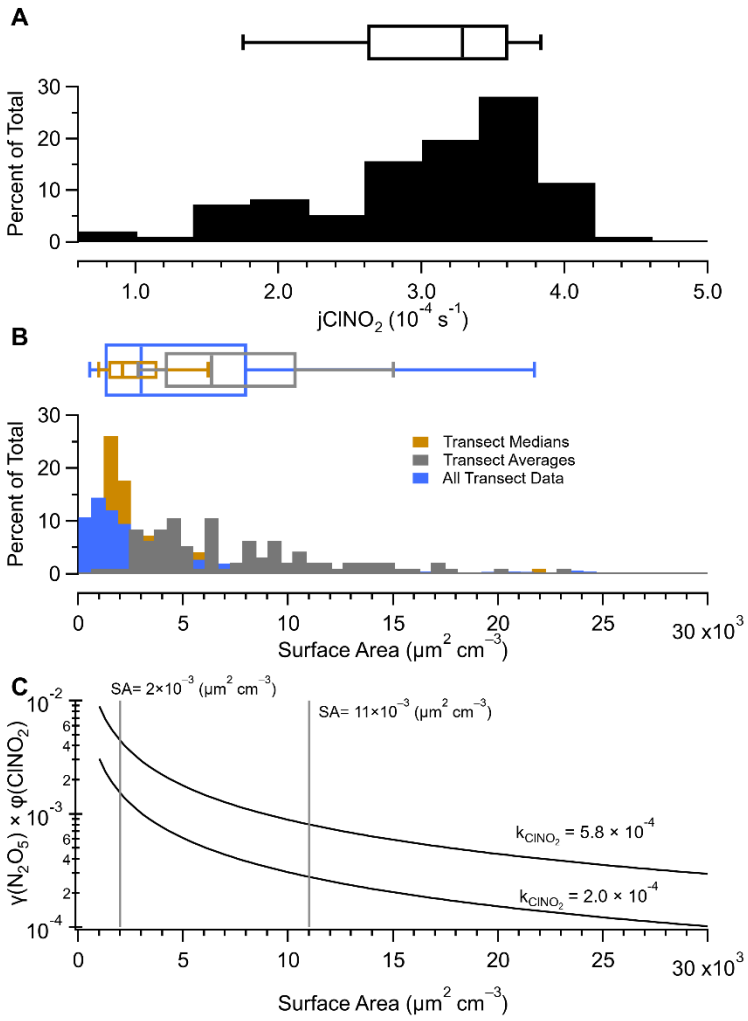

Figure S6. (A) Histogram of observed photolysis rates of $ClNO_2$ ($jClNO_2$) for calculated NEMR in Figure 3A. (B) Histograms of the aerosol surface area in the agricultural-fueled fires sampled by the DC-8 during FIREX-AQ. The transect medians (grey) and averages (brown) represent a median or average of single transects. This is compared to all transect data (blue), which shows all smoke data. Box and whiskers show results for the 10th, 25th, 50th, 75th, and 90th percentiles. In (A) and (B) box and whiskers show results for the 10th, 25th, 50th, 75th, and 90th percentiles. (C) A sensitivity analysis of $\gamma(N_2O_5) \times \varphi(ClNO_2)$ as a function of aerosol surface area. The region between grey vertical lines represents our best estimate range of $\gamma(N_2O_5) \times \varphi(ClNO_2)$ based on a range of aerosol surface area (SA) and the observed $kClNO_2$ in Figure 3A.

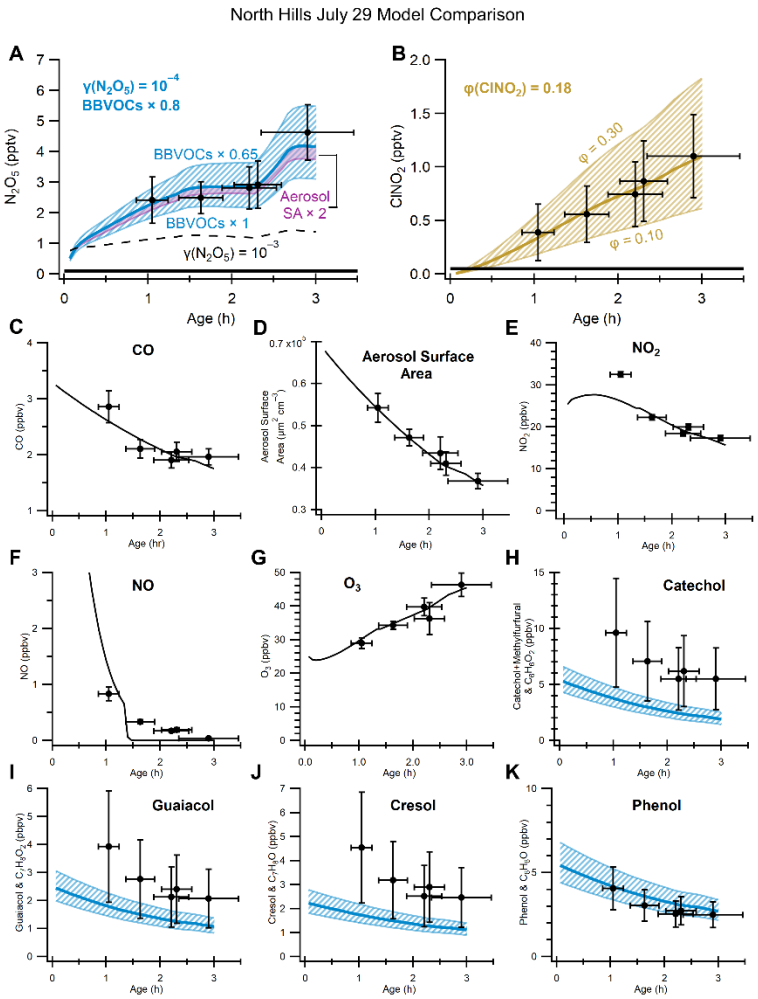

Figure S7. Comparison of box model results to observations for the North Hills Fire on July 29. Observations are shown as black markers while model results are shown as solid lines. Vertical error bars include instrument uncertainty and 1-σ variability (added in quadrature: the square root of the sum of squares) of the average of the transect center observations (observations aligned with the top 5% of CO). The blue shading in H–K corresponds to model results shown in A.

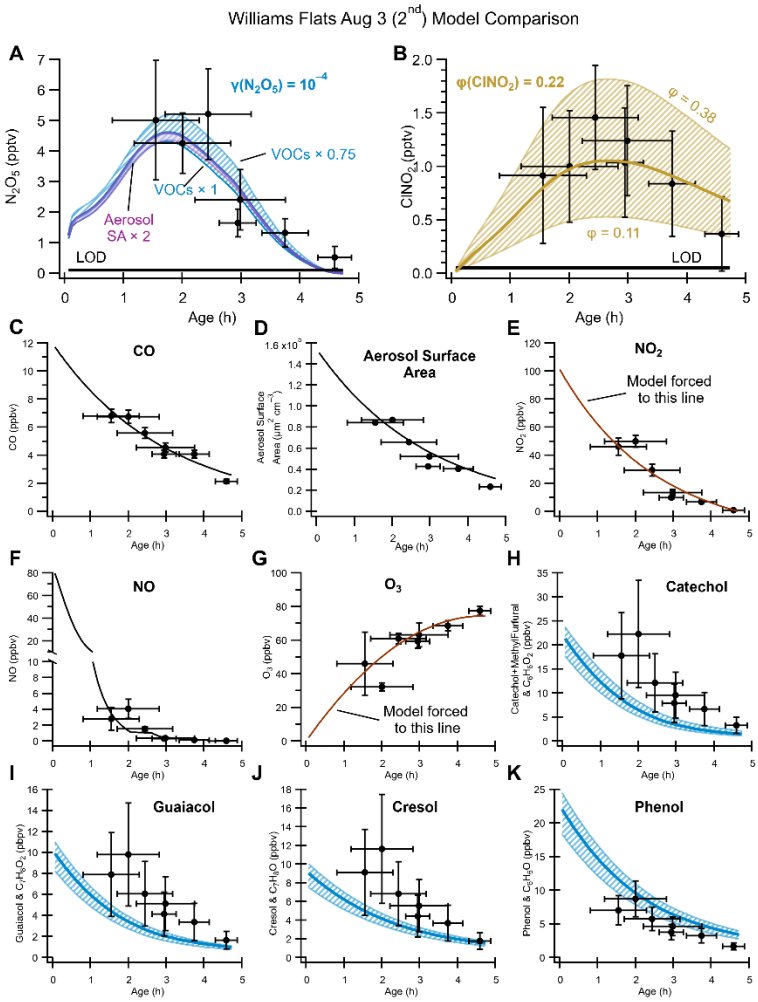

Figure S8. Comparison of box model results to observations for the Williams Flats fire on Aug 3 (2nd sampling). Observations are shown as black markers while model results are shown as solid lines. Vertical error bars include instrument uncertainty and 1-σ variability (added in quadrature: the square root of the sum of squares) of the average of the transect center observations (observations aligned with the top 5% of CO). The blue shading in H–K corresponds to model results shown in A. In this model, red lines indicate when a compound was forced to a guiding line as it was unable to be reproduced by the model for reasons discussed in Decker et al.(2)

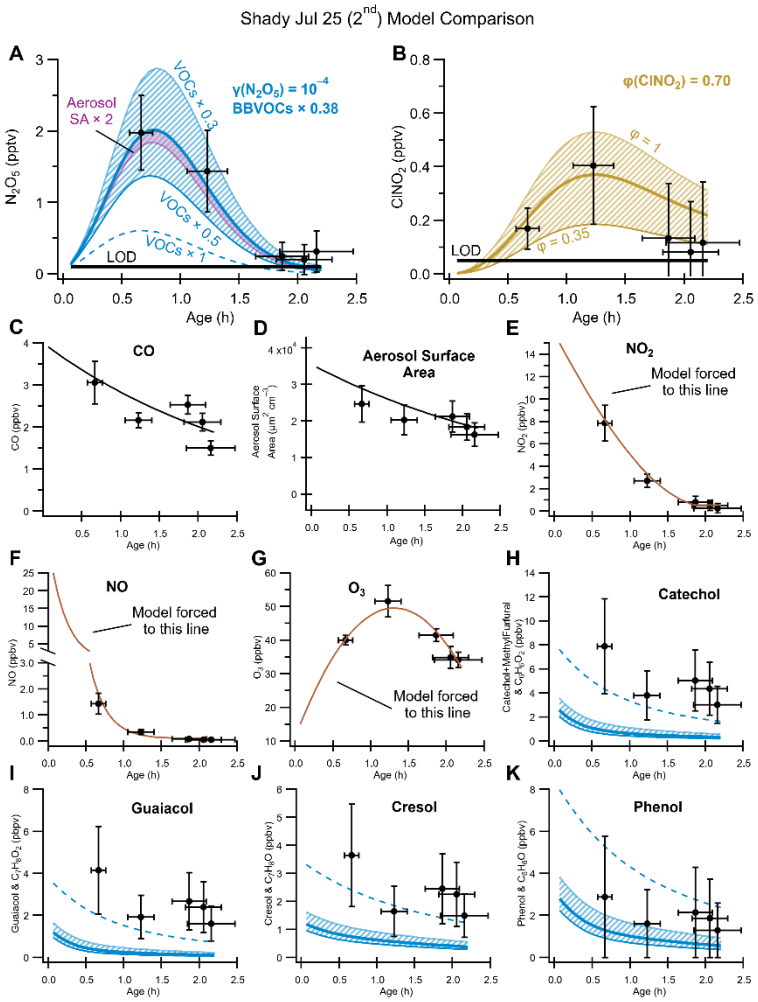

Figure S9. Comparison of box model results to observations for the Shady fire on July 25 (2nd sampling). Observations are shown as black markers while model results are shown as solid lines. Vertical error bars include instrument uncertainty and 1-σ variability (added in quadrature: the square root of the sum of squares) of the average of the transect center observations (observations aligned with the top 5% of CO). The blue shading in H–K corresponds to model results shown in A. In this model, red lines indicate when a compound was forced to a guiding line as it was unable to be reproduced by the model for reasons discussed in Decker et al.(2)

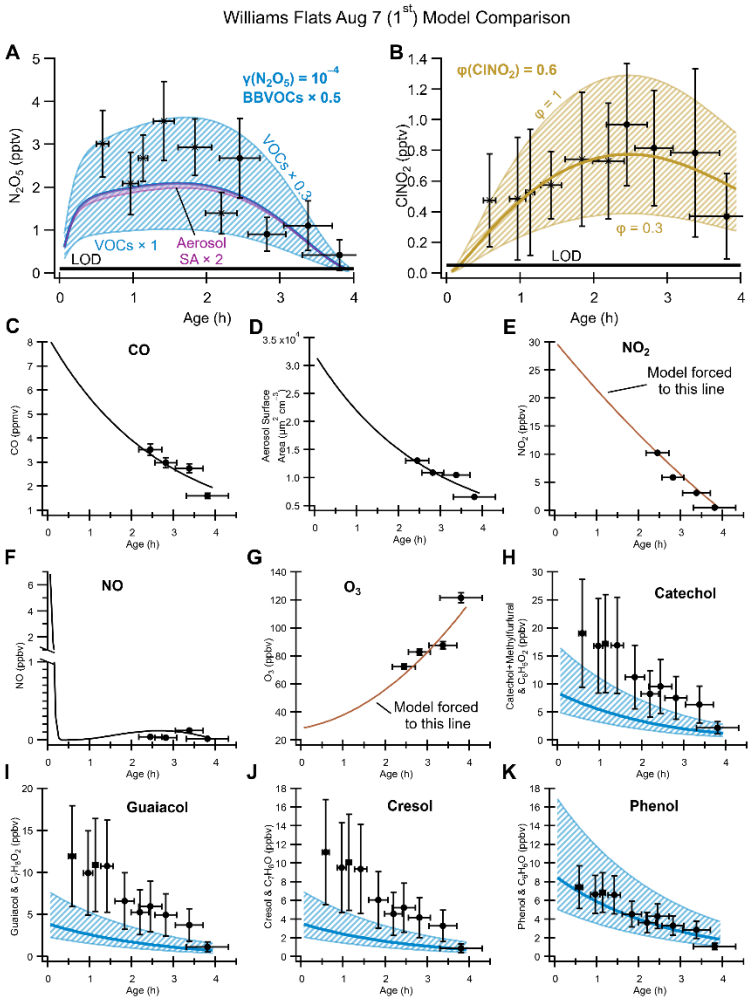

Figure S10. Comparison of box model results to observations for the Williams Flats fire on Aug 7 (1st sampling). Observations are shown as black markers while model results are shown as solid lines. Vertical error bars include instrument uncertainty and 1-σ variability (added in quadrature: the square root of the sum of squares) of the average of the transect center observations (observations aligned with the top 5% of CO). The blue shading in H–K corresponds to model results shown in A. In this model, red lines indicate when a compound was forced to a guiding line as it was unable to be reproduced by the model for reasons discussed in Decker et al.(2)

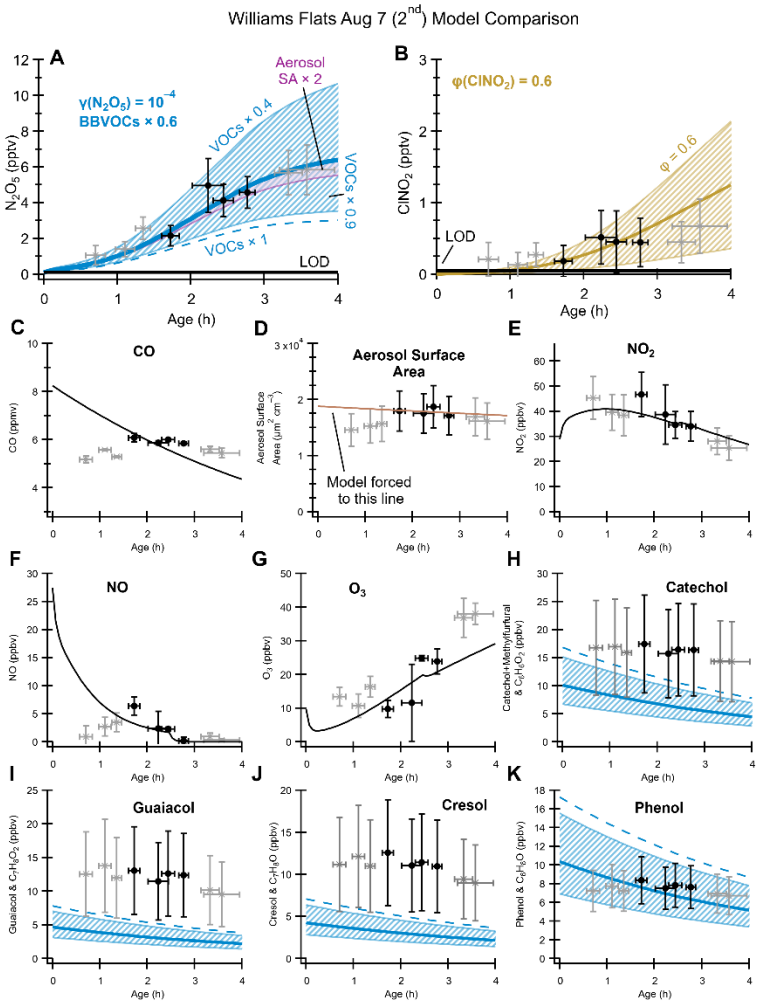

Figure S11. Comparison of box model results to observations for the Williams Flats fire on Aug 7 (2nd sampling). Observations are shown as markers while model results are shown as solid lines. Grey markers indicate observation excluded from the model for reasons discussed in Decker et al.(2) Vertical error bars include instrument uncertainty and 1-σ variability (added in quadrature: the square root of the sum of squares) of the average of the transect center observations (observations aligned with the top 5% of CO). The blue shading in H–K corresponds to model results corresponding shown in A. In this model, red lines indicate when a compound was forced to a guiding line as it was unable to be reproduced by the model for reasons discussed in Decker et al.(2)

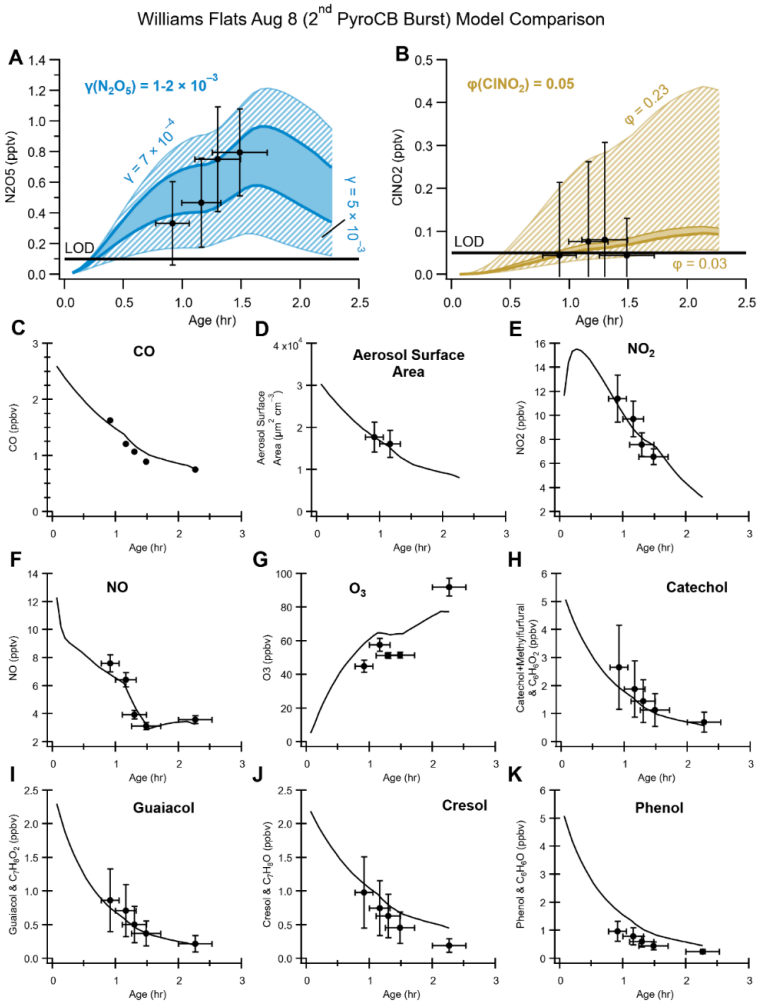

Figure S12. Comparison of box model results to observations for the Williams Flats fire on Aug 8 (2nd PyroCB burst). Error bars include instrument error with 1-σ uncertainty from the average of the transect center in added in quadrature (the square root of the sum of squares) observations as well as plume age uncertainty.

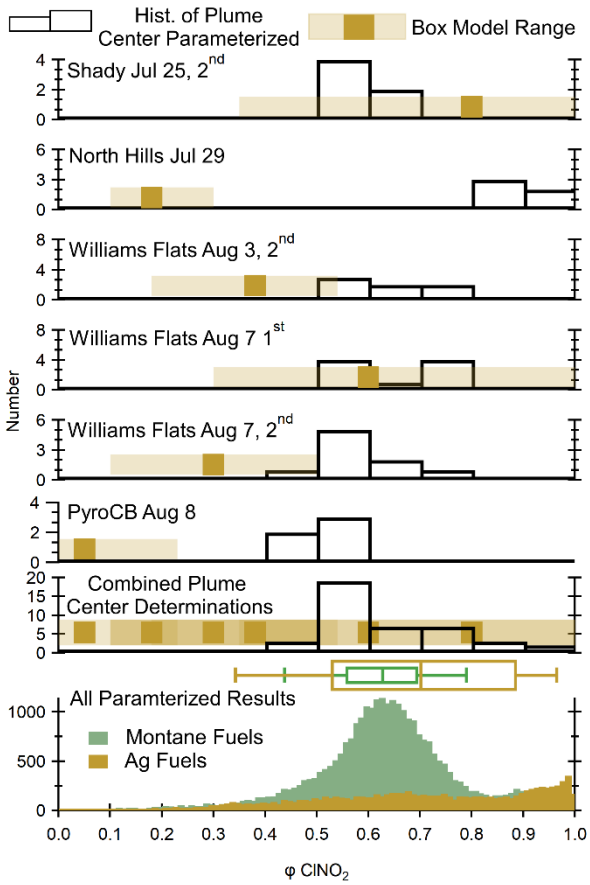

Figure S13. Comparison of the box model derived φ($ClNO_2$) for five montane plumes and the PyroCB event compared with parametrized φ($ClNO_2$). Box model derived values are shown as the gold horizontal bars. Parameterized φ($ClNO_2$) is shown in the histograms (vertical bars) for the transect center observations used in the box model (hollow bars) and for all observations from FIREX-AQ (solid bars). Box and whiskers show results for the 10th, 25th, 50th, 75th, and 90th percentiles.

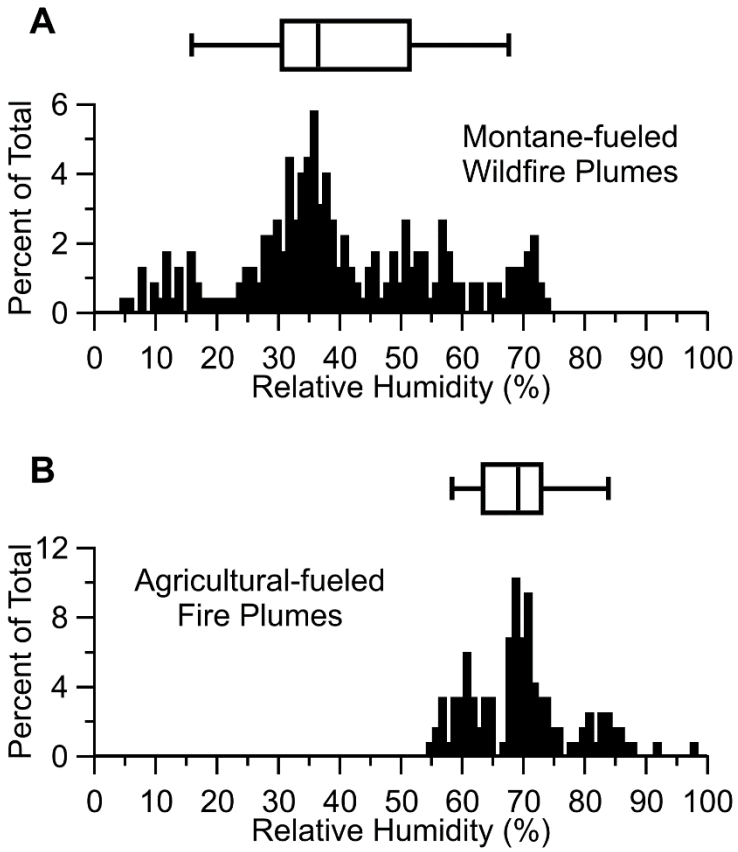

Figure S14. (A) and (B) show histograms of plume transect averaged relative humidity (RH). Each plume transect is averaged and combined as a histogram. For Montane-fueled wildfire plumes the average RH is 40% and the median is 36%. For agricultural-fueled plumes the average is 70% and the median is 69%. Box and whiskers show results for the 10^{th}, 25^{th}, 50^{th}, 75^{th}, and 90^{th} percentiles.

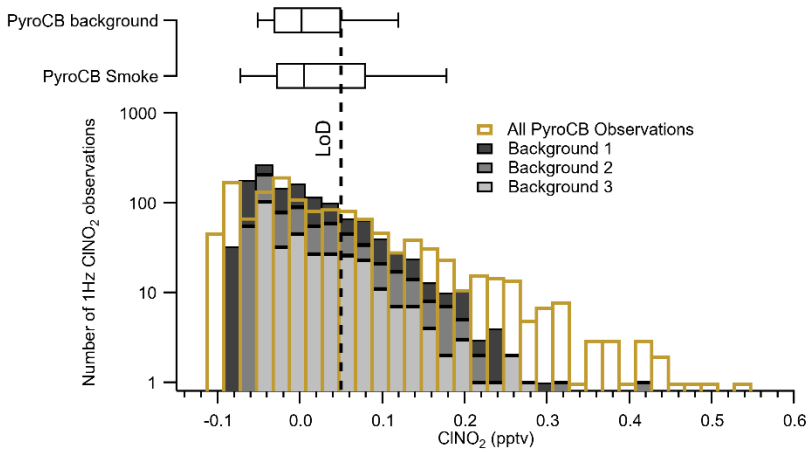

Figure S15. Histogram of $ClNO_2$ observations from the NOAA I^- CIMS on Aug 8 while sampling the PyroCB. The grey fill is stacked and indicates measurements taken from three background regions: one before the first measurement of PyroCB smoke, one after

the last measurement, and one in between two PyroCB transects. The transparent gold bars indicate measurements within the smoke. Box and whiskers show results for the 10th, 25th, 50th, 75th, and 90th percentiles. The median/average ± σ for plume $ClNO_2$ mixing ratios is 0.01 / 0.03 ± 0.10 pptv. The median/average ± σ for background $ClNO_2$ mixing ratios is 0.00 / 0.02 ± 0.06 pptv. The two averages are statistically different ($p < 0.001$).

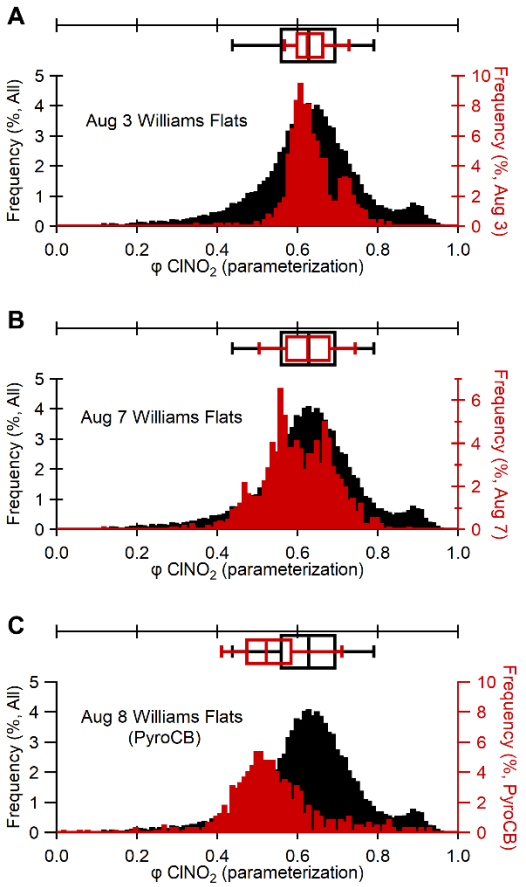

Figure S16. Comparison of parameterized φ($ClNO_2$) values for samplings of the Williams Flats fire smoke on three different days including the PyroCB on Aug 8. Results in black represent all observed wildfire smoke while observations in red show the Williams Flats fire sampled on Aug 3 (**A**) with a median of 0.62, on Aug 7 (**B**) with a median of 0.63, and on Aug 8 (PyroCB event, **C**) with a median of 0.52. Box and whiskers show results for the 10th, 25th, 50th, 75th, and 90th percentiles.

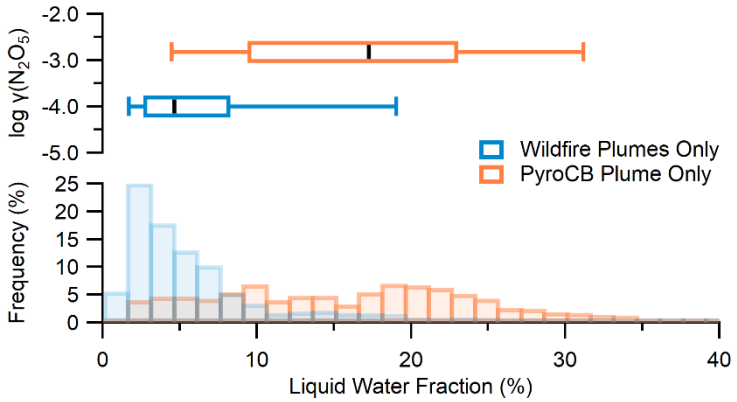

Figure S17. Comparison of liquid water fraction for all modeled wildfires except the PyroCB (blue) and only the PyroCB (orange). Liquid water fraction is defined as the liquid water content mass divided by the sum mass of the organic, ammonium, chloride, nitrate, sulfate, and liquid water). The box and whisker plots show the $\gamma(N_2O_5)$ as a function of liquid water content with 10th, 25th, 50th, 75th, and 90th percentiles shown. The histograms show the frequency of observations as a function of liquid water fraction. The median liquid water fraction for the wildfire plumes was 5%. The median liquid water fraction for the PyroCB was 17%).

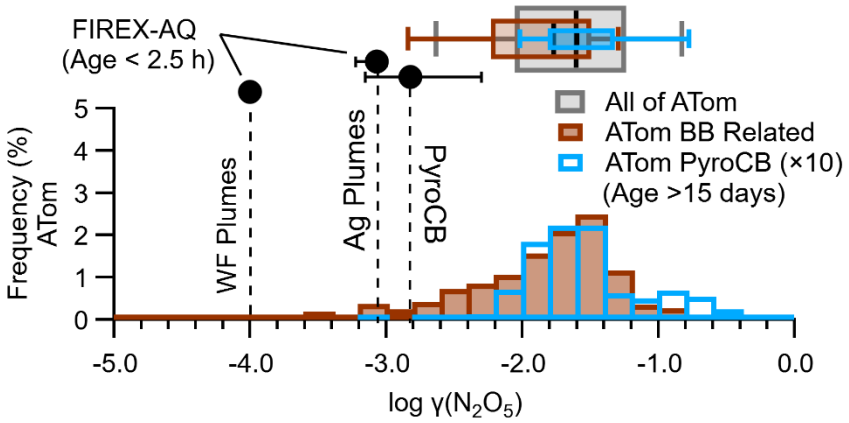

Figure S18. Comparison of the model-derived or fitted $\gamma(N_2O_5)$ values from FIREX-AQ and ATom as shown in Figure 5A, but with the addition of a subset of data identified by Katich et al. (33) in ATom-3 to have PyroCB influence. Markers show FIREX-AQ results, and the histograms show ATom BB-related $\gamma(N_2O_5)$ values. The box and whisker plots show the ATom BB-related (brown) (Methods), ATom-3 aerosol with PyroCB influence (33) (blue), and all of the ATom (grey) results from the UTLS.

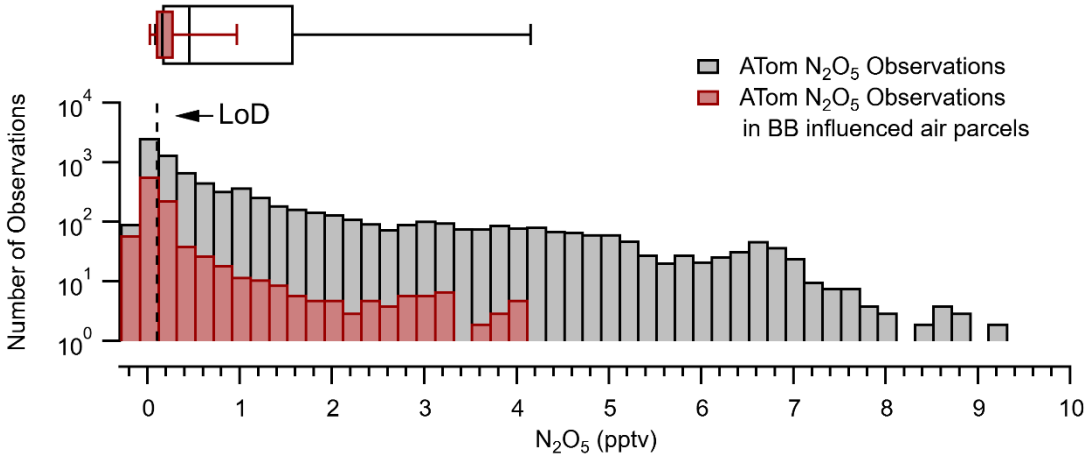

Figure S19. Observations of N_2O_5 (pptv) from the NOAA I^- CIMS aboard the NASA DC-8 during the ATom campaign. Grey bars indicate all observations while red bars indicate observations in BB influenced air. The median/average ± σ for BB influenced N_2O_5 mixing ratios during ATom is 0.16 / 0.38 ± 0.71. The median/average ± σ for all N_2O_5 mixing ratios during ATom is 0.45 / 1.27 ± 1.82.

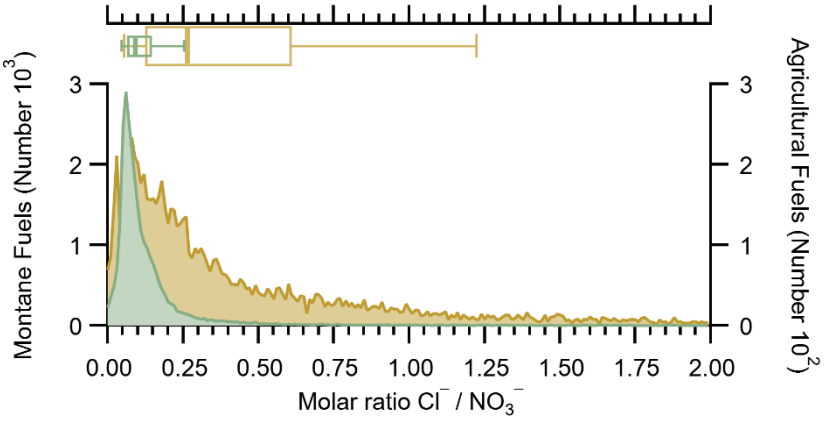

Figure S20. Histograms of the molar ratio of aerosol Cl^- to NO_3^- for montane fueled smoke (green) and agricultural-fueled smoke (brown). The montane-fueled smoke median/average ± σ is 0.1 / 0.1 ± 0.2 and the agricultural fueled smoke median/average ± σ is 0.3 / 0.4 ± 0.4. Box plots show 10th, 25th, 50th, 75th, and 90th percentiles.

Measurements Used	Method	Platform	Campaign	Sample Frequency
CO	Picarro G2401-m, cavity ringdown spectrometer.	Twin Otter	FIREX-AQ	0.5 Hz
Non-refractory PM_1 chemical composition	ECCC aircraft High-resolution Aerosol Mass Spectrometer (HR-AMS)	Twin Otter	FIREX-AQ	1 Hz
CO	Tunable diode laser spectrometer	DC-8	FIREX-AQ	1 Hz
CO	Cavity enhanced spectrometer	DC-8	FIREX-AQ	1 Hz
NO_2, NO_y, and O_3	NOAA chemiluminescence	DC-8	FIREX-AQ ATom	1 Hz
NO_2, HONO	NOAA broadband Airborne Cavity Enhanced Spectrometer (ACES)	DC-8	FIREX-AQ	1 Hz
NO	NOAA laser induced fluorescence	DC-8	FIREX-AQ	1 Hz
$C_6H_6O_2$, C_6H_6O, C_7H_8O, $C_7H_8O_2$.	NOAA Proton Transfer Reaction Time of Flight Mass Spectrometer	DC-8	FIREX-AQ	1 Hz
$C_6H_6O_2$, C_6H_6O, C_7H_8O, $C_7H_8O_2$.	University of Innsbruck Proton Transfer Reaction Time of Flight Mass Spectrometer	DC-8	FIREX-AQ	1 Hz
HONO, N_2O_5, $ClNO_2$	NOAA Iodide Time of Flight Chemical Ionization Mass Spectrometer (I^- ToF CIMS)	DC-8	FIREX-AQ ATom (N_2O_5)	1 Hz
Aerosol Size Distribution and Derived Surface Area	Scanning mobility particle sizer (SMPS) Laser Aerosol Spectrometer (LAS)	DC-8	FIREX-AQ	60 sec 1 Hz
Non-refractory PM_1 chemical composition	CU aircraft High Resolution Aerosol Mass Spectrometer (HR-AMS)	DC-8	FIREX-AQ ATom	1 Hz
Photolysis rates	Charged-coupled device Actinic Flux Spectroradiometer (CAFS)	DC-8	FIREX-AQ ATom	1-5 Hz 1-3 Hz
bulk aerosol size distributions	Combination of techniques for dry diameters 2.7 nm – 4.8 μm	DC-8	ATom	1 Hz
Identification of cloud periods	Cloud, Aerosol, and Precipitation Spectrometer (CAPS)	DC-8	ATom	1 Hz
Identification of pyrogenic-influenced aerosol	Particle Analysis by Laser Mass Spectrometry (PALMS)	DC-8	ATom	1Hz

Table S1. Table of instrumentation used in this work.

	Transects used for the NEMR calculation	Transects rejected for the NEMR calculation
N_2O_5 (Agricultural)	15	68
$ClNO_2$ (Agricultural)	90	29
N_2O_5 (Montane)	95	104
$ClNO_2$ (Montane)	70	98

Table S2. A count of transects used or rejected for the calculation of N_2O_5 or $ClNO_2$. Roughly 37 % and 46 % of plume transects included N_2O_5 and $ClNO_2$, respectively, well in excess of the instrumental detection limits (LoD: N_2O_5=0.1 pptv and $ClNO_2$=0.05 pptv at 1 Hz).

Fire name	State	Latitude	Longitude	Date sampled	Time sampled	Fuel
Shady Fire	Idaho	44.52	-115.02	July 24	17:45–18:15 MDT	Timber, Tall grass, and Logging debris
Sheep Fire	Idaho	43.56	-112.88	July 24	16:15–16:30 MDT	Sage-grass, Juniper, Grass, and Sagebrush
North Hills	Montana	46.75	-111.96	July 29	20:45–21:45 MDT	Managed Xeric, Understory, Sagebrush, Shrubland
Williams Flats	Washington	47.94	-118.62	Aug 03	17:30–19:30 PDT	Short grass, Ponderosa timber
				Aug 07	16:30–17:45 PDT & 18:00–19:30 PDT	
				Aug 08	17:45–19:15 PDT	

Table S3. List of wildfires referenced in the main text. A complete list of fires from FIREX-AQ is found in [*Warneke et al.*, 2023].

References

Ahern, A. T., L. Goldberger, L. Jahl, J. Thornton, and R. C. Sullivan (2018), Production of N_2O_5 and $ClNO_2$ through Nocturnal Processing of Biomass-Burning Aerosol, *Environmental Science & Technology*, *52*(2), 550-559, 10.1021/acs.est.7b04386.

Akagi, S. K., R. J. Yokelson, C. Wiedinmyer, M. J. Alvarado, J. S. Reid, T. Karl, J. D. Crounse, and P. O. Wennberg (2011), Emission factors for open and domestic biomass burning for use in atmospheric models, *Atmos. Chem. Phys.*, *11*(9), 4039-4072, 10.5194/acp-11-4039-2011.

Bertram, T. H., J. A. Thornton, and T. P. Riedel (2009), An experimental technique for the direct measurement of N2O5 reactivity on ambient particles, *Atmos. Meas. Tech.*, *2*(2), 231-242.

Bloss, C., V. Wagner, M. E. Jenkin, R. Volkamer, W. J. Bloss, J. D. Lee, D. E. Heard, K. Wirtz, M. Martin-Reviejo, G. Rea, J. C. Wenger, and M. J. Pilling (2005), Development of a detailed chemical mechanism (MCMv3.1) for the atmospheric oxidation of aromatic hydrocarbons, *Atmos. Chem. Phys.*, *5*(3), 641-664, 10.5194/acp-5-641-2005.

Brock, C. A., C. Williamson, A. Kupc, K. D. Froyd, F. Erdesz, N. Wagner, M. Richardson, J. P. Schwarz, R. S. Gao, J. M. Katich, P. Campuzano-Jost, B. A. Nault, J. C. Schroder, J. L. Jimenez, B. Weinzierl, M. Dollner, T. Bui, and D. M. Murphy (2019), Aerosol size distributions during the Atmospheric Tomography Mission (ATom): methods, uncertainties, and data products, *Atmos. Meas. Tech.*, *12*(6), 3081-3099, 10.5194/amt-12-3081-2019.

Decker, Z. C. J., M. A. Robinson, K. C. Barsanti, I. Bourgeois, M. M. Coggon, J. P. DiGangi, G. S. Diskin, F. M. Flocke, A. Franchin, C. D. Fredrickson, G. I. Gkatzelis, S. R. Hall, H. Halliday, C. D. Holmes, L. G. Huey, Y. R. Lee, J. Lindaas, A. M. Middlebrook, D. D. Montzka, R. Moore, J. A. Neuman, J. B. Nowak, B. B. Palm, J. Peischl, F. Piel, P. S. Rickly, A. W. Rollins, T. B. Ryerson, R. H. Schwantes, K. Sekimoto, L. Thornhill, J. A. Thornton, G. S. Tyndall, K. Ullmann, P. Van Rooy, P. R. Veres, C. Warneke, R. A. Washenfelder, A. J. Weinheimer, E. Wiggins, E. Winstead, A. Wisthaler, C. Womack, and S. S. Brown (2021), Nighttime and daytime dark oxidation chemistry in wildfire plumes: an observation and model analysis of FIREX-AQ aircraft data, *Atmos. Chem. Phys.*, *21*(21), 16293-16317, 10.5194/acp-21-16293-2021.

Fountoukis, C., and A. Nenes (2007), ISORROPIA II: a computationally efficient thermodynamic equilibrium model for K⁺–Ca²⁺–Mg²⁺–NH₄⁺–Na⁺–SO₄^{2−}–NO₃[−]–Cl[−]–H₂O aerosols, *Atmos. Chem. Phys.*, *7*(17), 4639-4659, 10.5194/acp-7-4639-2007.

Guo, H., L. Xu, A. Bougiatioti, K. M. Cerully, S. L. Capps, J. R. Hite Jr, A. G. Carlton, S. H. Lee, M. H. Bergin, N. L. Ng, A. Nenes, and R. J. Weber (2015), Fine-particle water and pH in the southeastern United States, *Atmos. Chem. Phys.*, *15*(9), 5211-5228, 10.5194/acp-15-5211-2015.

Guo, H., P. Campuzano-Jost, B. A. Nault, D. A. Day, J. C. Schroder, D. Kim, J. E. Dibb, M. Dollner, B. Weinzierl, and J. L. Jimenez (2021), The importance of size ranges

in aerosol instrument intercomparisons: a case study for the Atmospheric Tomography Mission, *Atmos. Meas. Tech.*, *14*(5), 3631-3655, 10.5194/amt-14-3631-2021.

Koss, A. R., K. Sekimoto, J. B. Gilman, V. Selimovic, M. M. Coggon, K. J. Zarzana, B. Yuan, B. M. Lerner, S. S. Brown, J. L. Jimenez, J. Krechmer, J. M. Roberts, C. Warneke, R. J. Yokelson, and J. de Gouw (2018), Non-methane organic gas emissions from biomass burning: identification, quantification, and emission factors from PTR-ToF during the FIREX 2016 laboratory experiment, *Atmos. Chem. Phys.*, *18*(5), 3299-3319, 10.5194/acp-18-3299-2018.

Lao, M., L. R. Crilley, L. Salehpoor, T. C. Furlani, I. Bourgeois, J. A. Neuman, A. W. Rollins, P. R. Veres, R. A. Washenfelder, C. C. Womack, C. J. Young, and T. C. VandenBoer (2020), A portable, robust, stable, and tunable calibration source for gas-phase nitrous acid (HONO), *Atmos. Meas. Tech.*, *13*(11), 5873-5890, 10.5194/amt-13-5873-2020.

Lee, B. H., F. D. Lopez-Hilfiker, P. R. Veres, E. E. McDuffie, D. L. Fibiger, T. L. Sparks, C. J. Ebben, J. R. Green, J. C. Schroder, P. Campuzano-Jost, S. Iyer, E. L. D'Ambro, S. Schobesberger, S. S. Brown, P. J. Wooldridge, R. C. Cohen, M. N. Fiddler, S. Bililign, J. L. Jimenez, T. Kurtén, A. J. Weinheimer, L. Jaegle, and J. A. Thornton (2018), Flight Deployment of a High-Resolution Time-of-Flight Chemical Ionization Mass Spectrometer: Observations of Reactive Halogen and Nitrogen Oxide Species, *Journal of Geophysical Research: Atmospheres*, *123*(14), 7670-7686, https://doi.org/10.1029/2017JD028082.

Liggio, J., S.-M. Li, K. Hayden, Y. M. Taha, C. Stroud, A. Darlington, B. D. Drollette, M. Gordon, P. Lee, P. Liu, A. Leithead, S. G. Moussa, D. Wang, J. O'Brien, R. L. Mittermeier, J. R. Brook, G. Lu, R. M. Staebler, Y. Han, T. W. Tokarek, H. D. Osthoff, P. A. Makar, J. Zhang, D. L. Plata, and D. R. Gentner (2016), Oil sands operations as a large source of secondary organic aerosols, *Nature*, *advance online publication*, 10.1038/nature17646
http://www.nature.com/nature/journal/vaop/ncurrent/abs/nature17646.html#supplementary-information.

Liu, X., Y. Zhang, L. G. Huey, R. J. Yokelson, Y. Wang, J. L. Jimenez, P. Campuzano-Jost, A. J. Beyersdorf, D. R. Blake, Y. Choi, J. M. St. Clair, J. D. Crounse, D. A. Day, G. S. Diskin, A. Fried, S. R. Hall, T. F. Hanisco, L. E. King, S. Meinardi, T. Mikoviny, B. B. Palm, J. Peischl, A. E. Perring, I. B. Pollack, T. B. Ryerson, G. Sachse, J. P. Schwarz, I. J. Simpson, D. J. Tanner, K. L. Thornhill, K. Ullmann, R. J. Weber, P. O. Wennberg, A. Wisthaler, G. M. Wolfe, and L. D. Ziemba (2016), Agricultural fires in the southeastern U.S. during SEAC4RS: Emissions of trace gases and particles and evolution of ozone, reactive nitrogen, and organic aerosol, *Journal of Geophysical Research: Atmospheres*, *121*(12), 7383-7414, 10.1002/2016JD025040.

May, A. A., G. R. McMeeking, T. Lee, J. W. Taylor, J. S. Craven, I. Burling, A. P. Sullivan, S. Akagi, J. L. Collett Jr, M. Flynn, H. Coe, S. P. Urbanski, J. H. Seinfeld, R. J. Yokelson, and S. M. Kreidenweis (2014), Aerosol emissions from prescribed fires in the United States: A synthesis of laboratory and aircraft measurements, *Journal of Geophysical Research: Atmospheres*, *119*(20), 11,826-811,849, https://doi.org/10.1002/2014JD021848.

McDuffie, E., E. L. Fibiger Dorothy, P. Dubé William, F. Lopez-Hilfiker, H. Lee Ben, A. Thornton Joel, V. Shah, L. Jaeglé, H. Guo, J. Weber Rodney, J. Michael Reeves, J. Weinheimer Andrew, C. Schroder Jason, P. Campuzano-Jost, L. Jimenez Jose, E. Dibb Jack, P. Veres, C. Ebben, L. Sparks Tamara, J. Wooldridge Paul, C. Cohen Ronald, S. Hornbrook Rebecca, C. Apel Eric, T. Campos, R. Hall Samuel, K. Ullmann, and S. S. Brown (2018a), Heterogeneous N2O5 Uptake During Winter: Aircraft Measurements During the 2015 WINTER Campaign and Critical Evaluation of Current Parameterizations, *Journal of Geophysical Research: Atmospheres*, *123*(8), 4345-4372, 10.1002/2018JD028336.

McDuffie, E. E., D. L. Fibiger, W. P. Dubé, F. Lopez Hilfiker, B. H. Lee, L. Jaeglé, H. Guo, R. J. Weber, J. M. Reeves, A. J. Weinheimer, J. C. Schroder, P. Campuzano-Jost, J. L. Jimenez, J. E. Dibb, P. Veres, C. Ebben, T. L. Sparks, P. J. Wooldridge, R. C. Cohen, T. Campos, S. R. Hall, K. Ullmann, J. M. Roberts, J. A. Thornton, and S. S. Brown (2018b), $ClNO_2$ Yields From Aircraft Measurements During the 2015 WINTER Campaign and Critical Evaluation of the Current Parameterization, *Journal of Geophysical Research: Atmospheres*, *123*(22), 12,994-913,015, 10.1029/2018JD029358.

Müller, M., T. Mikoviny, S. Feil, S. Haidacher, G. Hanel, E. Hartungen, A. Jordan, L. Märk, P. Mutschlechner, R. Schottkowsky, P. Sulzer, J. H. Crawford, and A. Wisthaler (2014), A compact PTR-ToF-MS instrument for airborne measurements of volatile organic compounds at high spatiotemporal resolution, *Atmos. Meas. Tech.*, *7*(11), 3763-3772, 10.5194/amt-7-3763-2014.

Neuman, J. A., M. Trainer, S. S. Brown, K. E. Min, J. B. Nowak, D. D. Parrish, J. Peischl, I. B. Pollack, J. M. Roberts, T. B. Ryerson, and P. R. Veres (2016), HONO emission and production determined from airborne measurements over the Southeast U.S, *Journal of Geophysical Research: Atmospheres*, *121*(15), 9237-9250, 10.1002/2016JD025197.

Rickards, A. M. J., R. E. H. Miles, J. F. Davies, F. H. Marshall, and J. P. Reid (2013), Measurements of the Sensitivity of Aerosol Hygroscopicity and the κ Parameter to the O/C Ratio, *The Journal of Physical Chemistry A*, *117*(51), 14120-14131, 10.1021/jp407991n.

Roberts, J. M., H. D. Osthoff, S. S. Brown, and A. R. Ravishankara (2009), Laboratory studies of products of N_2O_5 uptake on Cl- containing substrates, *Geophys. Res. Lett.*, *36*, L20808, doi:10.1029/2009GL040448.

Schill, G. P., K. D. Froyd, H. Bian, A. Kupc, C. Williamson, C. A. Brock, E. Ray, R. S. Hornbrook, A. J. Hills, E. C. Apel, M. Chin, P. R. Colarco, and D. M. Murphy (2020), Widespread biomass burning smoke throughout the remote troposphere, *Nature Geoscience*, *13*(6), 422-427, 10.1038/s41561-020-0586-1.

Solomon, S., K. Stone, P. Yu, D. M. Murphy, D. Kinnison, A. R. Ravishankara, and P. Wang (2023), Chlorine activation and enhanced ozone depletion induced by wildfire aerosol, *Nature*, *615*(7951), 259-264, 10.1038/s41586-022-05683-0.

Thaler, R. D., L. H. Mielke, and H. D. Osthoff (2011), Quantification of Nitryl Chloride at Part Per Trillion Mixing Ratios by Thermal Dissociation Cavity Ring-Down Spectroscopy, *Analytical Chemistry*, *83*(7), 2761-2766, 10.1021/ac200055z.

Thompson, C. R., S. C. Wofsy, M. J. Prather, P. A. Newman, T. F. Hanisco, T. B. Ryerson, D. W. Fahey, E. C. Apel, C. A. Brock, W. H. Brune, K. Froyd, J. M.

Katich, J. M. Nicely, J. Peischl, E. Ray, P. R. Veres, S. Wang, H. M. Allen, E. Asher, H. Bian, D. Blake, I. Bourgeois, J. Budney, T. P. Bui, A. Butler, P. Campuzano-Jost, C. Chang, M. Chin, R. Commane, G. Correa, J. D. Crounse, B. Daube, J. E. Dibb, J. P. DiGangi, G. S. Diskin, M. Dollner, J. W. Elkins, A. M. Fiore, C. M. Flynn, H. Guo, S. R. Hall, R. A. Hannun, A. Hills, E. J. Hintsa, A. Hodzic, R. S. Hornbrook, L. G. Huey, J. L. Jimenez, R. F. Keeling, M. J. Kim, A. Kupc, F. Lacey, L. R. Lait, J.-F. Lamarque, J. Liu, K. McKain, S. Meinardi, D. O. Miller, S. A. Montzka, F. L. Moore, E. J. Morgan, D. M. Murphy, L. T. Murray, B. A. Nault, J. A. Neuman, L. Nguyen, Y. Gonzalez, A. Rollins, K. Rosenlof, M. Sargent, G. Schill, J. P. Schwarz, J. M. S. Clair, S. D. Steenrod, B. B. Stephens, S. E. Strahan, S. A. Strode, C. Sweeney, A. B. Thames, K. Ullmann, N. Wagner, R. Weber, B. Weinzierl, P. O. Wennberg, C. J. Williamson, G. M. Wolfe, and L. Zeng (2022), The NASA Atmospheric Tomography (ATom) Mission: Imaging the Chemistry of the Global Atmosphere, *Bulletin of the American Meteorological Society*, *103*(3), E761-E790, 10.1175/BAMS-D-20-0315.1.

Veres, P. R., J. A. Neuman, T. H. Bertram, E. Assaf, G. M. Wolfe, C. J. Williamson, B. Weinzierl, S. Tilmes, C. R. Thompson, A. B. Thames, J. C. Schroder, A. Saiz-Lopez, A. W. Rollins, J. M. Roberts, D. Price, J. Peischl, B. A. Nault, K. H. Møller, D. O. Miller, S. Meinardi, Q. Li, J.-F. Lamarque, A. Kupc, H. G. Kjaergaard, D. Kinnison, J. L. Jimenez, C. M. Jernigan, R. S. Hornbrook, A. Hills, M. Dollner, D. A. Day, C. A. Cuevas, P. Campuzano-Jost, J. Burkholder, T. P. Bui, W. H. Brune, S. S. Brown, C. A. Brock, I. Bourgeois, D. R. Blake, E. C. Apel, and T. B. Ryerson (2020), Global airborne sampling reveals a previously unobserved dimethyl sulfide oxidation mechanism in the marine atmosphere, *Proceedings of the National Academy of Sciences*, *117*(9), 4505, 10.1073/pnas.1919344117.

Wagner, N. L., W. P. Dubé, R. A. Washenfelder, C. J. Young, I. B. Pollack, T. B. Ryerson, and S. S. Brown (2011), Diode laser-based cavity ring-down instrument for NO_3, N_2O_5, NO, NO_2 and O_3 from aircraft, *Atmos. Meas. Tech.*, *4*, 1227-1240.

Warneke, C., J. P. Schwarz, J. Dibb, O. Kalashnikova, G. Frost, J. Al-Saad, S. S. Brown, W. A. Brewer, A. Soja, F. C. Seidel, R. A. Washenfelder, E. B. Wiggins, R. H. Moore, B. E. Anderson, C. Jordan, T. I. Yacovitch, S. C. Herndon, S. Liu, T. Kuwayama, D. Jaffe, N. Johnston, V. Selimovic, R. Yokelson, D. M. Giles, B. N. Holben, P. Goloub, I. Popovici, M. Trainer, A. Kumar, R. B. Pierce, D. Fahey, J. Roberts, E. M. Gargulinski, D. A. Peterson, X. Ye, L. H. Thapa, P. E. Saide, C. H. Fite, C. D. Holmes, S. Wang, M. M. Coggon, Z. C. J. Decker, C. E. Stockwell, L. Xu, G. Gkatzelis, K. Aikin, B. Lefer, J. Kaspari, D. Griffin, L. Zeng, R. Weber, M. Hastings, J. Chai, G. M. Wolfe, T. F. Hanisco, J. Liao, P. Campuzano Jost, H. Guo, J. L. Jimenez, J. Crawford, and F.-A. Q. S. T. The (2023), Fire Influence on Regional to Global Environments and Air Quality (FIREX-AQ), *Journal of Geophysical Research: Atmospheres*, *128*(2), e2022JD037758, https://doi.org/10.1029/2022JD037758.

Wofsy, S. C., S. Afshar, H. M. Allen, E. C. Apel, E. C. Asher, B. Barletta, J. Bent, H. Bian, B. C. Biggs, D. R. Blake, N. Blake, I. Bourgeois, C. A. Brock, W. H. Brune, J. W. Budney, T. P. Bui, A. Butler, P. Campuzano-Jost, C. S. Chang, M. Chin, R. Commane, G. Correa, J. D. Crounse, P. D. Cullis, B. C. Daube, D. A. Day, J. M.

Dean-Day, J. E. Dibb, J. P. DiGangi, G. S. Diskin, M. Dollner, J. W. Elkins, F. Erdesz, A. M. Fiore, C. M. Flynn, K. D. Froyd, D. W. Gesler, S. R. Hall, T. F. Hanisco, R. A. Hannun, A. J. Hills, E. J. Hintsa, A. Hoffman, R. S. Hornbrook, L. G. Huey, S. Hughes, J. L. Jimenez, B. J. Johnson, J. M. Katich, R. F. Keeling, M. J. Kim, A. Kupc, L. R. Lait, J.-F. Lamarque, J. Liu, K. McKain, R. J. Mclaughlin, S. Meinardi, D. O. Miller, S. A. Montzka, F. L. Moore, E. J. Morgan, D. M. Murphy, L. T. Murray, B. A. Nault, J. A. Neuman, P. A. Newman, J. M. Nicely, X. Pan, W. Paplawsky, J. Peischl, M. J. Prather, D. J. Price, E. A. Ray, J. M. Reeves, M. Richardson, A. W. Rollins, K. H. Rosenlof, T. B. Ryerson, E. Scheuer, G. P. Schill, J. C. Schroder, J. P. Schwarz, J. M. St.Clair, S. D. Steenrod, B. B. Stephens, S. A. Strode, C. Sweeney, D. Tanner, A. P. Teng, A. B. Thames, C. R. Thompson, K. Ullmann, P. R. Veres, N. Vieznor, N. L. Wagner, A. Watt, R. Weber, B. Weinzierl, P. O. Wennberg, C. J. Williamson, J. C. Wilson, G. M. Wolfe, C. T. Woods, and L. H. Zeng (2018), ATom: Merged Atmospheric Chemistry, Trace Gases, and Aerosols, in *ORNL DAAC*, edited, Oak Ridge, Tennessee, USA.

Wolfe, G. M., M. R. Marvin, S. J. Roberts, K. R. Travis, and J. Liao (2016), The Framework for 0-D Atmospheric Modeling (F0AM) v3.1, *Geosci. Model Dev.*, *9*(9), 3309-3319, 10.5194/gmd-9-3309-2016.